Geophysical Research Letters

RESEARCH LETTER
10.1029/2018GL079019

Key Points:
- Atmospheric rivers are evaluated in the ECMWF Integrated Forecasting System and AR Reconnaissance dropsonde observations
- Atmospheric river structure is well captured by ECMWF model
- Water vapor flux errors are most related to uncertainties in the winds near the top of the planetary boundary layer

Correspondence to:
D. A. Lavers,
david.lavers@ecmwf.int

Citation:
Lavers, D. A., Rodwell, M. J., Richardson, D. S., Ralph, F. M., Doyle, J. D., Reynolds, C. A., et al. (2018). The gauging and modeling of rivers in the sky. *Geophysical Research Letters*, *45*, 7828–7834. https://doi.org/10.1029/2018GL079019

Received 4 JUN 2018
Accepted 20 JUL 2018
Accepted article online 25 JUL 2018
Published online 8 AUG 2018

The Gauging and Modeling of Rivers in the Sky

David A. Lavers[1], Mark J. Rodwell[1], David S. Richardson[1], F. Martin Ralph[2], James D. Doyle[3], Carolyn A. Reynolds[3], Vijay Tallapragada[4], and Florian Pappenberger[1]

[1]European Centre for Medium-Range Weather Forecasts (ECMWF), Reading, UK, [2]Center for Western Weather and Water Extremes (CW3E), Scripps Institution of Oceanography, University of California, San Diego, CA, USA, [3]Naval Research Laboratory, Monterey, CA, USA, [4]NOAA/NWS/NCEP/Environmental Modeling Center, College Park, MD, USA

Abstract Atmospheric rivers (ARs) are responsible for most of the horizontal water vapor flux outside of the tropics and can cause extreme precipitation and affect the atmospheric dynamics and predictability. For their impacts to be skillfully predicted, it is essential for weather forecasting systems to accurately represent AR characteristics. Using the European Centre for Medium-Range Weather Forecasts Integrated Forecasting System and dropsonde observations from the 2018 AR Reconnaissance field campaign over the Northeast Pacific Ocean, it is shown that the AR structure is modeled well but that short-range water vapor flux forecasts have a root-mean-square error of 60.0 kgm^{-1} s^{-1} (21.9% of mean observed flux). These errors are most related to uncertainties in the winds near the top of the planetary boundary layer. The findings identify a potential barrier in the prediction of high-impact weather and suggest an area where research should be focused to improve atmospheric forecast systems.

Plain Language Summary Atmospheric rivers (ARs) are responsible for most of the horizontal transport of water vapor outside of the tropics and can cause extreme precipitation and affect the atmospheric circulation. In this study, we evaluate the ability of a state-of-the-science weather forecasting system to model ARs by using unique atmospheric observations from the 2018 AR Reconnaissance field campaign. Results show that while the AR structure is modeled well, there can be large errors in the water vapor transport which are most related to uncertainties in the low-level winds. These findings identify a potential barrier in the prediction of high-impact weather.

1. Introduction

Atmospheric rivers (ARs; Ralph et al., 2018) are responsible for most of the horizontal flux of water vapor outside of the tropics, with typical fluxes exceeding those of the Amazon River (Ralph et al., 2004, 2017; Zhu & Newell, 1998). These relatively long, narrow, and lower tropospheric features on the order of 2,000 km in length and 800 km in width generally form over the oceans and are situated in the precold frontal part of midlatitude cyclones (Ralph et al., 2005, 2017). ARs can be the cause of extreme precipitation, flooding, and adverse socioeconomic effects particularly in coastal mountainous regions (Lavers et al., 2011; Neiman et al., 2011; Ralph et al., 2006; Ramos et al., 2015), and they are important for water resources (Dettinger et al., 2011). Also, the latent heat release associated with ARs when their water vapor condenses can affect the atmospheric dynamics and predictability (Doyle et al., 2014; Schäfler & Harnisch, 2015). For these impacts to be skillfully predicted, it is essential for weather forecasting systems to be able to accurately represent the characteristics of ARs.

The process of weather forecasting, known as numerical weather prediction, involves the integration of numerical models that describe atmospheric and oceanic motion from an initial atmospheric state to determine future weather conditions (Bauer et al., 2015). A key ingredient for numerical weather prediction is the availability of global atmospheric observations, such as those from low Earth orbit and geostationary satellites, aircraft, radiosonde (balloon) ascents, ocean buoys, and ships. These observations are collected and then ingested into short-range (background) weather forecasts in a procedure called data assimilation to produce the best estimate (analysis) of the current atmospheric conditions; from this analysis, the new weather forecast is run. Because of uncertainties in the initial atmospheric state and due to inadequacies in the numerical model formulations themselves, multiple realizations of possible future atmospheric conditions or states are generated, a process called ensemble forecasting. At the European Centre for Medium-Range Weather Forecasts (ECMWF), the Integrated Forecasting System (IFS) operational ensemble of forecasts (ENS) are

produced 2 times per day to provide a quantitative assessment of the range of possible weather outcomes for the coming days. It is this ENS and the ensemble data assimilation system that are assessed herein.

Past research has shown that the IFS and other global weather models have skillful AR forecasts (Baggett et al., 2017; DeFlorio et al., 2018; Lavers et al., 2016, 2017; Mundhenk et al., 2018; Nayak et al., 2014; Wick et al., 2013). However, hitherto, no study has evaluated if the AR region in a weather forecasting system is subject to particular errors or uncertainties, and given the role of ARs in extreme events and atmospheric predictability, this is a critical research area. To undertake such an assessment, observations of ARs are required, and this represents a challenge because over the oceans where ARs mostly develop and occur, there are few in situ observations. Specifically, there are very few wind and moisture observations with the fidelity that adequately depict the horizontal and vertical structure of ARs. Thus, currently, the only approach to systematically observe the characteristics of ARs to allow for a model assessment is to have a targeted field campaign in which research aircraft deploy dropsondes (instruments that measure the atmospheric pressure, winds, water vapor, and temperature as they descend through the atmosphere; Ralph et al., 2017) to gauge AR conditions. These dropsondes are then ingested into forecast systems, such as the IFS, which allows for model evaluation. In part to allow for such an assessment, a field campaign called AR Reconnaissance (AR Recon) was organized for January and February 2018, and six intensive observation periods (IOPs) were conducted, five of which are discussed here.

2. Data and Methods

2.1. Intensive Observation Periods and Dropsonde Data

Six IOPs took place centered on 00UTC 27 January, 00UTC 29 January, 00UTC 1 February, 00UTC 3 February, 00UTC 26 February, and 00UTC 28 February 2018, with the specific aim that the dropsondes would mostly influence the 00 UTC analyses. Only five IOPs are used herein because the data for 26 February were not communicated in real time which prevented real-time assimilation. The IOPs had up to three research aircraft (with an average flight range of about 8 hr per aircraft) that each released dropsondes into ARs and other dynamically active areas. These data were then uploaded on to the World Meteorological Organization Global Telecommunications System and ingested in the data assimilation step of the ECMWF IFS. In order to perform a consistent comparison across IOPs and between the dropsonde observations and the IFS output, the assessment herein uses specific humidity and winds on the 700-, 850-, and 925-hPa standard pressure levels. This sampling resulted in the use of 319 dropsondes (86 in IOP1, 47 in IOP2, 76 in IOP3, 85 in IOP4, and 25 in IOP5).

2.2. ECMWF Ensemble of Data Assimilations and Forecasts

To consider the uncertainty in the initial atmospheric flow, an ensemble of data assimilations (EDA; Isaksen et al., 2010) is employed at ECMWF. Each of the 25 EDA members combines information from its background forecast with many millions of observations (including the dropsonde data from AR Recon). The variance of the EDA background forecasts provides information on the uncertainty in the background. Estimated observation errors are accounted for through different observation perturbations in each EDA member. The resulting 25 new analyses thus attempt to represent the remaining uncertainty in the current state. The ENS, which runs out to 15 days, is then used here to evaluate how uncertainty grows at longer lead times. The initial conditions for the 50 ENS members are obtained from a symmetric combination of 6-hr forecasts from the EDA analyses, the latest single high-resolution forecast, and singular vector perturbations (Lang et al., 2015). Data output from the EDA and the ENS are archived and were retrieved from the ECMWF Meteorological Archival and Retrieval System. In this study, EDA and ENS data were interpolated to the location of the dropsonde observations before comparisons were made.

2.3. Water Vapor Transport

The vertically integrated horizontal zonal and meridional water vapor transport components were calculated in a Eulerian framework; these were combined into the integrated vapor transport (IVT; Neiman et al., 2008). The IVT (observed and forecasted) at each dropsonde location was calculated assuming zero horizontal flux at the ocean surface and at 650 hPa and used the specific humidity and the zonal and meridional winds at 700, 850, 925, and 1,000 hPa where available (e.g., if the surface pressure $>$ 1,000 hPa). This is a reasonable approach as the majority of the IVT occurs at lower altitudes (Ralph et al., 2005), and this also guards

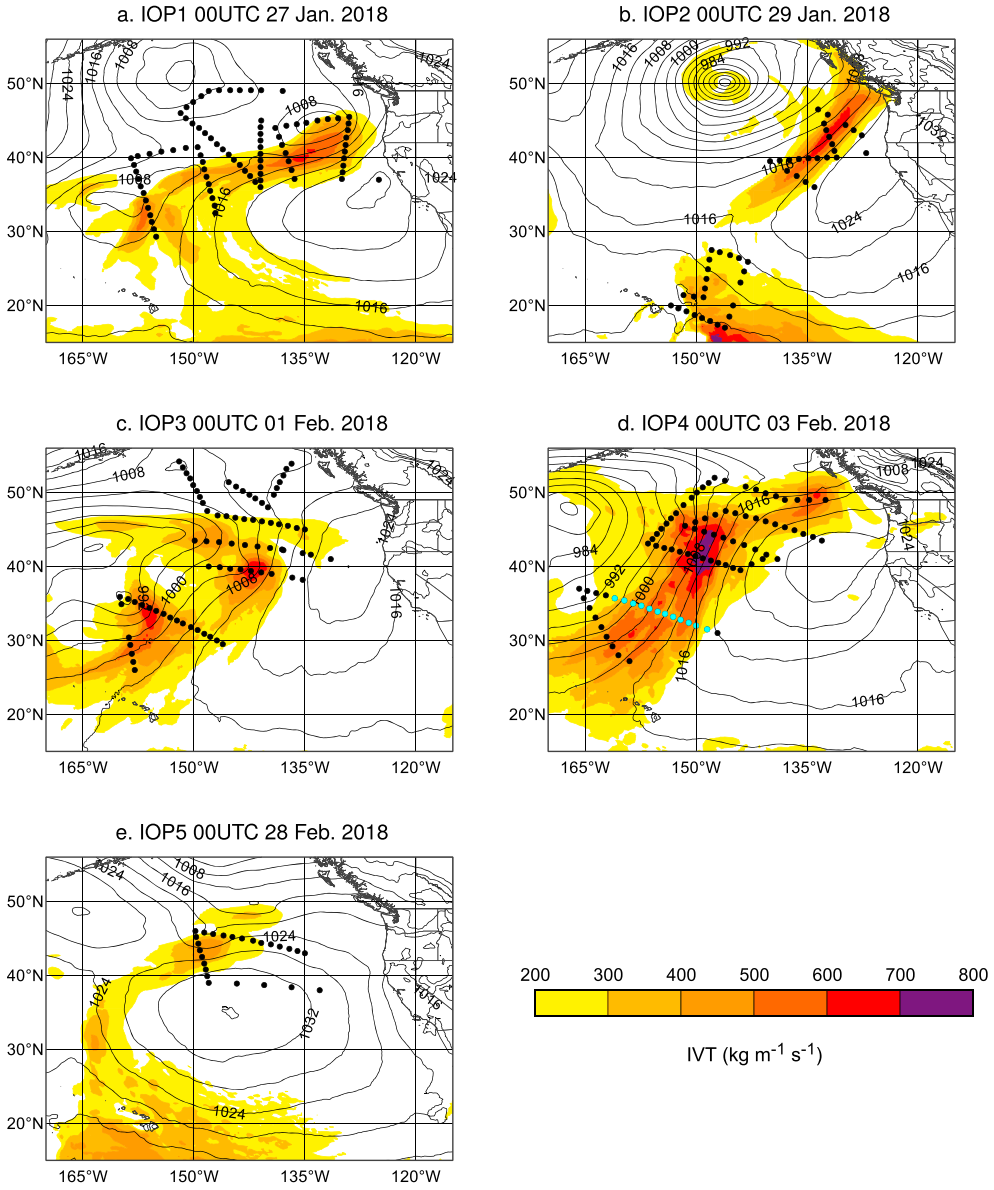

Figure 1. The five intensive observation periods. (a–e) The European Centre for Medium-Range Weather Forecasts analysis of mean sea level pressure and water vapor transport up to 650 hPa during the five intensive observation periods. Dropsonde locations, where data are available at 700, 850, and 925 hPa, are given by black dots, and the atmospheric river transect assessed in Figure 2 is given by cyan dots.

against any one pressure level exerting a disproportionate influence on the IVT calculation, thus allowing the diagnosis of potential model issues. To identify AR conditions in this study, an IVT > 200 kgm^{-1} s^{-1} is used. The standard deviation of the IVT forecasts, a measure of uncertainty, was evaluated as $\sqrt{\overline{Var(IVT)}}$, where the bar is the average over all dropsondes.

3. Results

Figure 1 shows the IVT, mean sea level pressure, and dropsonde locations during the five IOPs. The flight tracks and dropsonde locations were chosen to measure the atmospheric properties across areas predicted to have high IVT, and in particular within ARs, and to sample other dynamically active regions. To investigate the structure and strength of the ARs, the modeled and observed IVT at dropsonde locations along the flight transects were analyzed. In Figure 2a, for each of the 12 dropsondes along the AR transect given by cyan dots

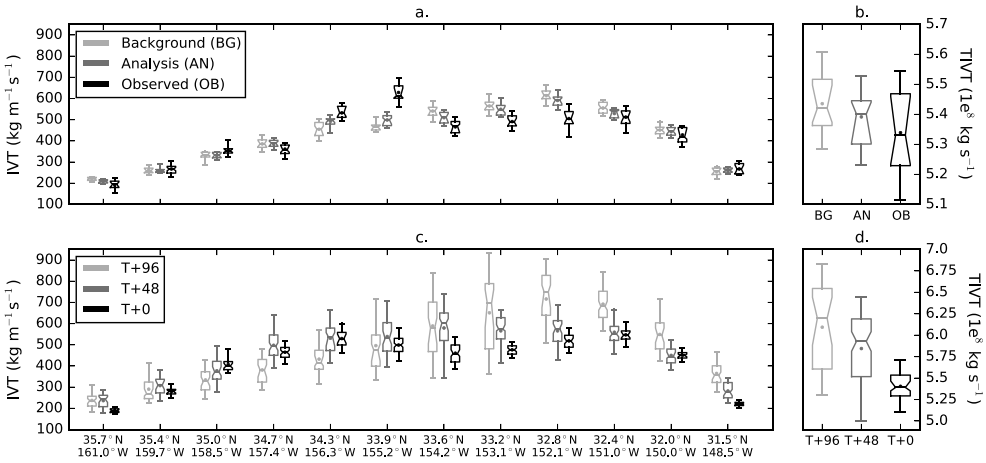

Figure 2. Example of an atmospheric river transect. (a) The integrated vapor transport (IVT) distribution in the 25 ensemble of data assimilations members of the background, analysis, and observation at each dropsonde across the atmospheric river (AR) as given by cyan dots in Figure 1d. (b) The distribution of the total IVT integrated across the AR. (c) The IVT distribution in the 50 ensemble members of the $T + 96$ forecasts, $T + 48$ forecasts, and $T + 0$ valid at 00UTC 3 February 2018. (d) The distribution of the total IVT integrated across the AR. The bottom and top of the boxes correspond to the 25th and 75th percentiles, respectively, the line in the box is the median, the dot in the box is the mean, and the whiskers represent the 5th and 95th percentiles. In the boxes, the notch shows the 95% confidence interval around the median from a 1,000 bootstrapped sample.

in Figure 1d, the IVT distribution of the 25 (1) background forecasts, (2) analyses, and (3) perturbed (dropsonde) observations that represent observation uncertainty is plotted. Along this transect, the spatial and temporal separation of the dropsondes are approximately 100 km and 12 min, respectively. Visual inspection of the positions of the box plots in Figure 2a suggests that the AR structure is well captured in the IFS at short time ranges (3 to 15 hr). It is also evident that the analysis generally draws away from the background and toward the observations, reflecting the blending of the model background with the observations during the data assimilation step. However, assessment of the IVT magnitudes highlights locations where large IVT differences exist, for example, at 33.9°N 155.2°W. The fact that there is no overlap between the background/analyses and observation at 33.9°N 155.2°W indicates that issues may exist in modeling the IVT magnitude. Furthermore, the variation between the dropsonde observations along the transect is larger than in the background or analysis, which may indicate model deficiencies in representing the fine-scale structure. For this same transect, Figure 2c shows the IVT distribution of the 50 ENS members on (1) day 4 ($T + 96$), (2) day 2 ($T + 48$), and (3) day 0 ($T + 0$) valid at 00UTC 3 February 2018. The general AR structure is visible in all of the forecasts. At $T + 0$, the method of initializing the ENS will, almost inevitably, lead to larger uncertainty than that of the EDA analyses. The tendency for larger forecast uncertainty with increasing lead time is confirmed by calculating the average ensemble spread over all 319 dropsondes; these are 27.8 kgm^{-1} s^{-1} for $T + 0$, 60.6 kgm^{-1} s^{-1} for $T + 48$, and 93.1 kgm^{-1} s^{-1} for $T + 96$. Note that as the uncertainty drops off toward the edges of the transect, this implies that the AR is generally in the correct location in the IFS, suggesting that the IVT errors may be originating from mesoscale rather than synoptic-scale processes. To provide a bulk flux perspective for the AR example given in Figure 2, the total flux across the AR is presented in Figures 2b and 2d. This shows similar mean values between the model and observations and quantifies the increasing uncertainty for the bulk flux.

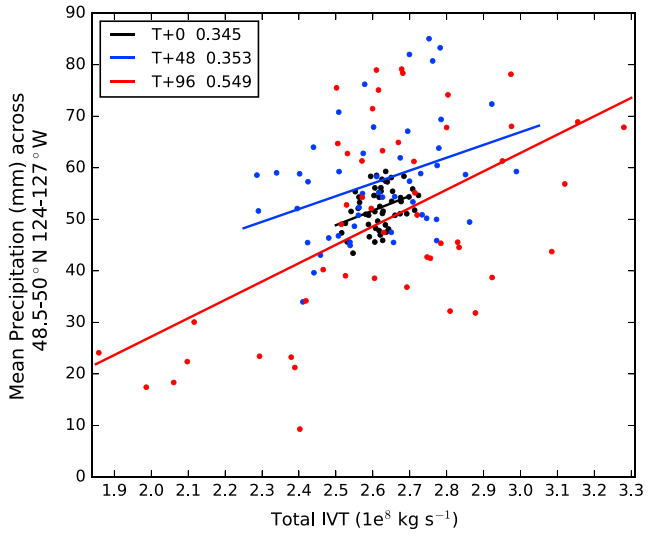

Figure 3. Relationship between integrated vapor transport (IVT) and rainfall in the 50 ensemble members. For IOP2, the total IVT flux valid at 00UTC 29 January 2018 averaged over the four transects nearest the North American Coast (Figure 1b) is plotted against the average model rainfall across southwestern Vancouver Island (48.5°N–50°N 124°W–127°W) valid for 00UTC 29 to 00UTC 30 January 2018. The black dots refer to IVT at $T + 0$ and rainfall accumulated from $T + 0$ to $T + 24$; the blue dots refer to IVT at $T + 48$ and rainfall accumulated from $T + 48$ to $T + 72$; the red dots refer to IVT at $T + 96$ and rainfall accumulated from $T + 96$ to $T + 120$. The linear regression lines are plotted, and the linear Pearson correlations (which are significant at the 0.05 level) are given in the legend.

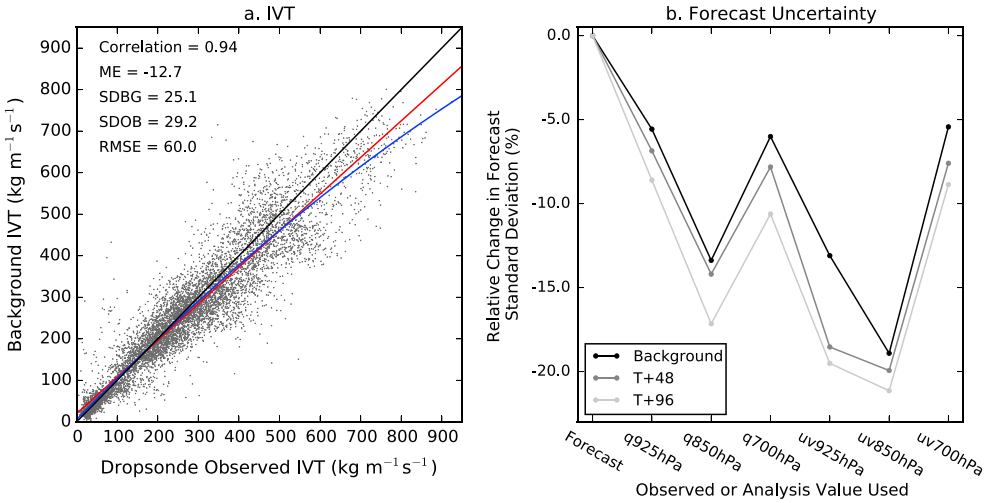

Figure 4. Uncertainty in integrated vapor transport (IVT) forecasts. (a) Scatterplot of the IVT in the 25 ensemble of data assimilations background and observed realizations at the 319 dropsondes (n = 7,975). The linear correlation, mean error (forecast-observed), standard deviation of the background forecasts, standard deviation of the perturbed observations, and the root-mean-square error are given. The 1:1 line is given in black, the linear regression line is in red, and the second degree polynomial line is in blue. (b) The relative change in IVT forecast standard deviation (%) compared to the forecast when replacing the forecast specific humidity q or winds uv at 925-, 850-, and 700-hPa levels with the unperturbed observation or unperturbed analysis value from the ensemble forecast system.

The IVT uncertainty found is important for high-impact weather along the coast. During IOP2, southwest British Columbia and Vancouver Island were hit with flooding and landslides due to the heavy rain. In Figure 3, the evaluation at T + 0, T + 48, and T + 96 of the mean model precipitation across 48.5°N–50°N 124°W–127°W and the total IVT flux averaged over the four transects nearest the North American Coast (Figure 1b) highlights the association between forecasted IVT and precipitation uncertainties in the 50 ENS members. The three regression lines are reasonably parallel with each other confirming a consistent relationship among the lead times, and the regression (and higher correlation) at T + 96 is likely to give a more robust indicator of the sensitivity as the IVT spans a wider range of values. Previous research has also shown a strong IVT relationship with precipitation (Rutz et al., 2014). Thus, by reducing these IVT uncertainties, improved forecasts for high-impact rainfall events may be possible.

It is now important to diagnose the origin of IVT differences between the model and observations so that potential model issues can be addressed. In Figure 4a, a scatterplot of the 25 realizations of the background and observed IVT at the 319 dropsonde locations (n = 7,975) highlights the strong linear correlation between them. There is a mean error of −12.7 kgm^{-1} s^{-1}, which is largely associated with the 850-hPa level, and the location of the linear regression (red) and second-order polynomial (blue) lines below the 1:1 line suggests a particular issue with higher IVT values. The estimated IVT uncertainty, as measured by the standard deviation, is 25.1 kgm^{-1} s^{-1} in the background forecasts and 29.2 kgm^{-1} s^{-1} in the observed IVT. These are all taken into account by the RMSE, and this shows an overall uncertainty of 60.0 kgm^{-1} s^{-1} (21.9% of the mean observed flux), and as with the mean error the biggest issues appear to occur at higher IVT values, which has implications for the most extreme precipitation events. To investigate what leads to the largest IVT uncertainties, the forecast values of the specific humidity or wind at each pressure level were replaced one at a time with the unperturbed observation or unperturbed analysis value from the ENS system, and the standard deviation of the IVT recalculated. In Figure 4b, the normalized reduction in the IVT forecast standard deviation (compared to the original forecast) is plotted for the background, day 2 (T + 48), and day 4 (T + 96) forecasts (valid close to the drop time of the dropsondes). It is evident that the 850-hPa winds contribute most to the IVT uncertainty at all lead times considered. The 925-hPa winds and 850-hPa specific humidity also lead to considerable uncertainty in the IVT. This suggests that the IVT uncertainty may partly be addressed through better initialization of the winds and moisture near the top of the planetary boundary layer. At higher altitudes at 700 hPa, there is a smaller change in the forecast standard deviation suggesting that uncertainties at this level are less critical for the IVT magnitude.

4. Conclusions

This study has used the ECMWF IFS and unique dropsonde observations from a targeted field campaign to show that first, the structure of ARs is well captured in the IFS, and second, that model errors do exist in the IVT, a key AR property. These modeled IVT errors largely originate from the top of and above the planetary boundary layer, especially at 850 hPa, and errors in the winds are found to be the source of the most IVT uncertainty. This finding identifies a potential model limitation in predicting high-impact extreme precipitation events driven by ARs and also implies that because the IVT has errors, the location of the water vapor, its condensation, and hence latent heat release are likely to be incorrectly placed in the IFS forecasts, which will affect the atmospheric dynamics and predictability. It is hypothesized that in addition to improvements in the model, the initialization of the forecasts could benefit from targeted airborne dropsondes in future AR Recon field campaigns and from extra space-based observations, such as from the proposed AEOLUS (Källén, 2008) observations of winds, and water vapor from the Meteosat Third Generation Infrared Sounder (Stuhlmann et al., 2009). This, in turn, could improve forecasts of ARs and the IVT. Also, an analysis using higher vertical resolution dropsonde and forecast data may further elucidate IVT uncertainties. Future field campaigns will enable new model comparisons to be undertaken to ascertain whether model improvements are benefiting the modeling of the IVT along the atmospheric branch of the global hydrological cycle.

Acknowledgments
The authors gratefully acknowledge financial support from the European Union Horizon 2020 IMPREX (grant agreement 641811) and ANYWHERE projects (grant agreement 700099). Computer support from Fernando Ii and comments by Aneesh Subramanian are also acknowledged. J.D.D. and C.A.R. acknowledge the support of the Chief of Naval Research through the NRL Base Program PE 0601153N. The data used are available on the ECMWF MARS server. We also thank the two anonymous reviewers for their comments.

References

Baggett, C. F., Barnes, E. A., Maloney, E. D., & Mundhenk, B. D. (2017). Advancing atmospheric river forecasts into subseasonal-to-seasonal time scales. *Geophysical Research Letters*, *44*, 7528–7536. https://doi.org/10.1002/2017GL074434

Bauer, P., Thorpe, A., & Brunet, G. (2015). The quiet revolution of numerical weather prediction. *Nature*, *525*(7567), 47–55. https://doi.org/10.1038/nature14956

DeFlorio, M. J., Waliser, D. E., Guan, B., Lavers, D. A., Ralph, F. M., & Vitart, F. (2018). Global assessment of atmospheric river prediction skill. *Journal of Hydrometeorology*, *19*(2), 409–426. https://doi.org/10.1175/JHM-D-17-0135.1

Dettinger, M. D., Ralph, F. M., Das, T., Neiman, P. J., & Cayan, D. (2011). Atmospheric rivers, floods, and the water resources of California. *Water*, *3*(2), 445–478. https://doi.org/10.3390/w3020445

Doyle, J. D., Amerault, C., Reynolds, C. A., & Reinecke, P. A. (2014). Initial condition sensitivity and predictability of a severe extratropical cyclone using a moist adjoint. *Monthly Weather Review*, *142*(1), 320–342. https://doi.org/10.1175/MWR-D-13-00201.1

Isaksen, L., Bonavita, M., Buizza, R., Fisher, M., Haseler, J., Leutbecher, M., & Raynaud, L. (2010). *Ensemble of data assimilations at ECMWF*, *ECMWF Technical Memorandum No. 636*. Reading, UK: ECMWF.

Källén, E. (2008). Special issue with manuscripts related to ESA's Atmospheric Dynamics Mission/Aeolus. *Tellus A*, *60*(2), 189–190. https://doi.org/10.1111/j.1600-0870.2007.00296.x

Lang, S. T. K., Bonavita, M., & Leutbecher, M. (2015). On the impact of re-centering initial conditions for ensemble forecasts. *Quarterly Journal of the Royal Meteorological Society*, *141*(692), 2571–2581. https://doi.org/10.1002/qj.2543

Lavers, D. A., Allan, R. P., Wood, E. F., Villarini, G., Brayshaw, D. J., & Wade, A. J. (2011). Winter floods in Britain are connected to atmospheric rivers. *Geophysical Research Letters*, *38*, L23803. https://doi.org/10.1029/2011GL049783

Lavers, D. A., Pappenberger, F., Richardson, D. S., & Zsoter, E. (2016). ECMWF extreme forecast index for water vapor transport: A forecast tool for atmospheric rivers and extreme precipitation. *Geophysical Research Letters*, *43*, 11,852–11,858. https://doi.org/10.1002/2016GL071320

Lavers, D. A., Zsoter, E., Richardson, D. S., & Pappenberger, F. (2017). An assessment of the ECMWF extreme forecast index for water vapor transport during boreal winter. *Weather and Forecasting*, *32*(4), 1667–1674. https://doi.org/10.1175/WAF-D-17-0073.1

Mundhenk, B., Barnes, E., Maloney, E., & Baggett, C. (2018). Skillful empirical subseasonal prediction of landfalling atmospheric river activity using the Madden-Julian Oscillation and quasi-biennial oscillation. *NPJ Climate and Atmospheric Science*, *1*, 7. https://doi.org/10.1038/s41612-017-0008-2

Nayak, M. A., Villarini, G., & Lavers, D. A. (2014). On the skill of numerical weather prediction models to forecast atmospheric rivers over the central United States. *Geophysical Research Letters*, *41*, 4354–4362. https://doi.org/10.1002/2014GL060299

Neiman, P. J., Ralph, F. M., Wick, G. A., Lundquist, J. D., & Dettinger, M. D. (2008). Meteorological characteristics and overland precipitation impacts of atmospheric rivers affecting the West Coast of North America based on eight years of SSM/I satellite observations. *Journal of Hydrometeorology*, *9*(1), 22–47. https://doi.org/10.1175/2007JHM855.1

Neiman, P. J., Schick, L. J., Ralph, F. M., Hughes, M., & Wick, G. A. (2011). Flooding in western Washington: The connection to atmospheric rivers. *Journal of Hydrometeorology*, *12*(6), 1337–1358. https://doi.org/10.1175/2011JHM1358.1

Ralph, F. M., Dettinger, M. D., Cairns, M. M., Galarneau, T. J., & Eylander, J. (2018). Defining "atmospheric river": How the glossary of meteorology helped resolve a debate. *Bulletin of the American Meteorological Society*, *99*(4), 837–839. https://doi.org/10.1175/BAMS-D-17-0157.1

Ralph, F. M., Iacobellis, S. F., Neiman, P. J., Cordeira, J. M., Spackman, J. R., Waliser, D. E., et al. (2017). Dropsonde observations of total integrated water vapor transport within North Pacific atmospheric rivers. *Journal of Hydrometeorology*, *18*(9), 2577–2596. https://doi.org/10.1175/JHM-D-17-0036.1

Ralph, F. M., Neiman, P. J., & Rotunno, R. (2005). Dropsonde observations in low-level jets over the northeastern Pacific Ocean from CALJET-1998 and PACJET-2001: Mean vertical-profile and atmospheric-river characteristics. *Monthly Weather Review*, *133*(4), 889–910. https://doi.org/10.1175/MWR2896.1

Ralph, F. M., Neiman, P. J., & Wick, G. A. (2004). Satellite and CALJET aircraft observations of atmospheric rivers over the eastern North Pacific Ocean during the El Niño winter of 1997/98. *Monthly Weather Review*, *132*(7), 1721–1745. https://doi.org/10.1175/1520-0493(2004)132<1721:SACAOO>2.0.CO;2

Ralph, F. M., Neiman, P. J., Wick, G. A., Gutman, S. I., Dettinger, M. D., Cayan, D. R., & White, A. B. (2006). Flooding on California's Russian River: Role of atmospheric rivers. *Geophysical Research Letters*, *33*, L13801. https://doi.org/10.1029/2006GL026689

Ramos, A. M., Trigo, R. M., Liberato, M. L. R., & Ricardo, T. (2015). Daily precipitation extreme events in the Iberian Peninsula and its association with atmospheric rivers. *Journal of Hydrometeorology*, *16*(2), 579–597. https://doi.org/10.1175/JHM-D-14-0103.1

Rutz, J. J., Steenburgh, W. J., & Ralph, F. M. (2014). Climatological characteristics of atmospheric rivers and their inland penetration over the western United States. *Monthly Weather Review*, *142*(2), 905–921. https://doi.org/10.1175/MWR-D-13-00168.1

Schäfler, A., & Harnisch, F. (2015). Impact of the inflow moisture on the evolution of a warm conveyor belt. *Quarterly Journal of the Royal Meteorological Society*, *141*(686), 299–310. https://doi.org/10.1002/qj.2360

Stuhlmann, R. Rodriguez A., Tjemkes S., Aminou D. M., Stark H., & Schumann W. (2009). "MTG-IRS: Status, specifications and technical concept," in Advances in Imaging, OSA Technical Digest (CD) (Optical Society of America, 2009), Paper FMC1. https://doi.org/10.1364/FTS.2009.FMC1

Wick, G. A., Neiman, P. J., & Ralph, F. M. (2013). Description and validation of an automated objective technique for identification and characterization of the integrated water vapor signature of atmospheric rivers. *IEEE Transactions on Geoscience and Remote Sensing*, *51*(4), 2166–2176. https://doi.org/10.1109/TGRS.2012.2211024

Zhu, Y., & Newell, R. E. (1998). A proposed algorithm for moisture fluxes from atmospheric rivers. *Monthly Weather Review*, *126*(3), 725–735. https://doi.org/10.1175/1520-0493(1998)126<0725:APAFMF>2.0.CO;2